Current Optics and Photonics
Vol. 4, No. 4, August 2020, pp. 293-301

ISSN: 2508-7266(Print) / ISSN: 2508-7274(Online)
DOI: https://doi.org/10.3807/COPP.2020.4.4.293

Chip-scale Temperature-compensated Superstructured Waveguide Bragg Grating Based Multiparametric Sensor

Naik Parrikar Vishwaraj[1]*, Chandrika Thondagere Nataraj[2], Ravi Prasad Kogravalli Jagannath[3], Prashanth Gurusiddappa[1]***, and Srinivas Talabattula[4]**

[1]*Department of Electronics and Communication Engineering, National Institute of Technology Goa, Ponda 403401, India*
[2]*Department of Electronics and Telecommunication Engineering, Siddaganga Institute of Technology, Tumakuru-Karnataka 572103, India*
[3]*Department Applied Sciences, National Institute of Technology Goa, Ponda 403401, India*
[4]*Department of Electrical Communication Engineering, Indian Institute of Science, Bangalore-Karnataka 560012, India*

(Received December 26, 2019 : revised February 27, 2020 : accepted March 16, 2020)

In this paper we propose and theoretically analyze a monolithic multiparametric sensor consisting of a superstructure of surface-relief waveguide Bragg gratings (WBGs), a micro-machined diaphragm, and a cantilever beam. Diaphragms of two different configurations, namely circular and square, are designed and analyzed separately for pressure measurement. The square diaphragm is then selected for further study, since it shows relatively higher sensitivity compared to the circular one, as it incurs more induced stress when any pressure is applied. The cantilever beam with a proof mass is designed to enhance the sensitivity for acceleration measurement. A unique mathematical method using coupled-mode theory and the transfer-matrix method is developed to design and analyze the shift in the Bragg wavelength of the superstructure configuration of the gratings, due to simultaneously applied pressure and acceleration. The effect of temperature on the wavelength shift is compensated by introducing another Bragg grating in the superstructure configuration. The measured sensitivities for pressure and acceleration are found to be 0.21 pm/Pa and 6.49 nm/g respectively.

Keywords : Waveguide Bragg gratings, Pressure sensor, Accelerometer, Optical sensors, MOEMS
OCIS codes : (060.3735) Fiber Bragg gratings; (120.5475) Pressure measurement; (130.2790) Guided waves; (130.3120) Integrated optics devices; (280.4788) Optical sensing and sensors

I. INTRODUCTION

In these days, fiber-Bragg-grating (FBG) sensors are used successfully for a broad spectrum of applications in automobiles, aerospace, and biosensing due to their multiplexed sensing capabilities, lightweight design, and compactness [1-5]. Measurements of pressure, temperature, and acceleration are critical in industrial applications, and subsequently there is high demand for integrated composite sensors [6, 7]. However, these are based on the piezoresistive principle of sensing, in which piezoresistive elements are placed over a diaphragm and cantilever beam to measure pressure and acceleration respectively. Compact, planar photonic components are being considered for such applications, due to their potential for large-scale integration and reduced fabrication cost.

Micro-opto-electro-mechanical systems (MOEMS), realized by combining silicon photonics with micro-electro-mechanical

*Corresponding author: rajparrikar@gmail.com, ORCID 0000-0003-0115-9200
**Corresponding author: tnchandrika@sit.ac.in, ORCID 0000-0001-5031-1104
***Corresponding author: grprashanth@nitgoa.ac.in, ORCID 0000-0002-2936-4188

Color versions of one or more of the figures in this paper are available online.

systems (MEMS), offer the advantages of a small device footprint, cheapness, batch-fabrication possibilities, and easier CMOS integration with less complexity. MOEMS pressure sensors using a Mach-Zehnder interferometer (MZI), ring resonator, directional coupler, and gratings have been reported [3, 8-10].

Waveguide Bragg gratings (WBGs) on the silicon-on-insulator (SOI) platform have attracted interest for optical communication and various sensing applications. WBGs were first demonstrated by Murphy *et al.* [1] in 2001. The Bragg gratings are realized by physically corrugating dielectric waveguides; their sensitivity is obtained by observing the shift in the reflection wavelength. This method of detection, using the shift in wavelength, is preferred over methods that utilize the change in intensity of propagated light, as the former is more immune to noise [11]. However, Bragg-grating-based sensors are equally sensitive to temperature as to the parameters being measured. Hence it remains a difficult task to discriminate between the shift in wavelength due to temperature change and that due to the parameter being measured. If the shift due to temperature is not compensated, a MOEMS sensor gives inaccurate results, so it is necessary to subtract the wavelength shift due to temperature effects, so that we can attribute the wavelength shift only to changes in the actual parameter being measured, such as pressure or acceleration. In earlier works a chirped grating and dual gratings have been proposed to compensate for the effect of temperature in pressure sensors [12, 13]. However, surface-relief waveguide Bragg gratings for monolithic multiparametric sensing with temperature compensation have not been addressed so far. In addition, so far there has been no unique mathematical model to analyze such systems theoretically. Such systems could be an affordable solution for automobile, aerospace, and health applications, since they could be easily manufactured using standard microfabrication technologies.

In this paper we propose a WBG-based monolithic multiparametric sensor that is immune to temperature aberrations, for both pressure and acceleration measurements. A unique mathematical model using coupled-mode theory and the transfer-matrix method is developed to design the configuration of the superstructure of surface-relief Bragg gratings. The proposed sensor is made up of a superstructure configuration of three identical surface-relief waveguide Bragg gratings, designed with distinct Bragg wavelengths. Two of these gratings are located respectively on a micromachined diaphragm structure and a cantilever beam structure, where pressure and acceleration are applied. The wavelength shifts of these gratings are proportional to both pressure and acceleration, along with temperature. The third grating is placed separately, and is sensitive only to temperature variations. We theoretically analyze the sensor for measuring pressure and acceleration simultaneously while providing temperature compensation. The analysis shows that there are distinct shifts in the Bragg wavelength when measuring pressure and acceleration.

II. SENSOR CONFIGURATION

Figure 1 gives the schematic representation of the proposed temperature-independent multiparametric sensor. It consists of three identical Bragg gratings (Grating 1, Grating 2, and Grating 3) in a superstructure configuration, with distinct Bragg wavelengths λ_1, λ_2, and λ_3 respectively. Grating 1 is located on the square diaphragm, and Grating 2 is placed on the cantilever beam with a proof mass to obtain high sensitivity, whereas Grating 3 is located away from the diaphragm and cantilever beam. The distance between gratings is 500 μm.

When pressure and acceleration are respectively applied to the diaphragm and the cantilever beam, the mechanical

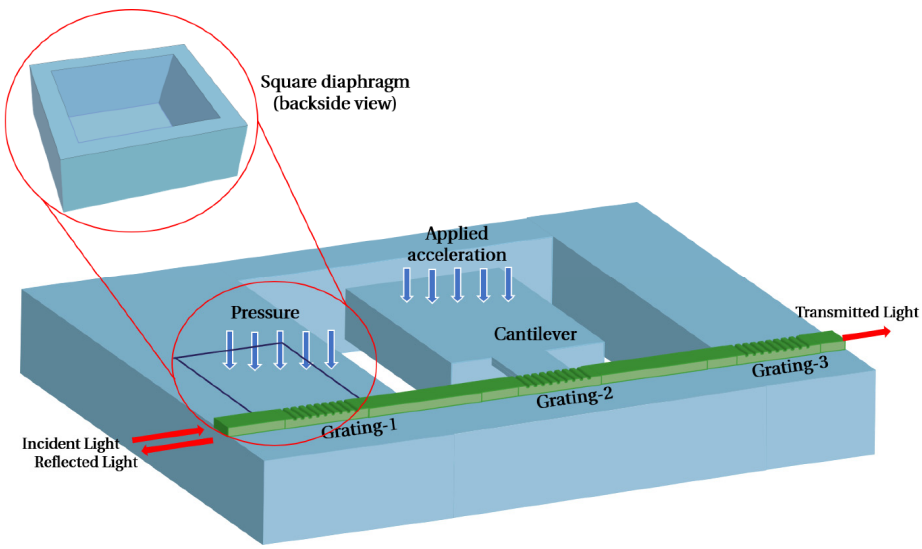

FIG. 1. Schematic diagram of a temperature-compensated, multiparametric WBG sensor.

displacement induces stress in the sensing structure. The effective refractive index (RI) and pitch of the grating varies as a result of this induced stress, which in turn leads to the shifts in the Bragg wavelengths of Grating 1 and Grating 2. Grating 3, however, is unaffected by the applied pressure and acceleration. Although the variation in temperature results in a Bragg-reflection-wavelength shift for all three gratings, this shift is equal, as the temperature change is the same for all the three gratings. While Grating 1 is affected by both pressure and temperature, Grating 3 is affected only by temperature. The difference between the two shifts eliminates the shift that is due purely to temperature. The same concept is applied for acceleration measurement also, wherein the difference of wavelength shifts between Grating 2 and Grating 3 is considered for temperature compensation.

III. THEORY AND DESIGN

The sensor design includes a superstructure grating, micro-machined diaphragm, cantilever beam, and optomechanical coupling between them.

3.1. Superstructure Surface-relief Waveguide Bragg Grating

The superstructure configuration consists of three surface-relief Bragg gratings connected by a waveguide between each pair, as shown in Fig. 2.

The surface-relief WBG consists of a silicon-slab waveguide, where the top surface is etched to obtain the periodic structure. Light propagates in the z-direction. The core material is silicon, and the cladding is air. The height of the waveguide is t, the grating depth is t_g, the length of the grating is L, and d is the ridge width, which is half of the grating pitch. Pitch can be calculated by using Bragg's equation:

$$\lambda_B = 2n_{eff}\Lambda, \tag{1}$$

where λ_B, n_{eff}, and Λ are Bragg's wavelength, the effective RI, and the pitch of the grating respectively. The transmitted and reflected fields are represented by a and b for light incident from the left, with the respective boundaries at $z=0$ and $z=L$. Only the fundamental mode and first-order diffraction are considered. Coupled-mode theory is used to analyze the WBG [14, 15].

As light propagates along a grating, partial reflections occur at each of the etchings, due to the surface etching of the waveguide. At the Bragg condition, the forward wave (transmitted field) and backward wave (reflected field) are in phase. As a result, coupling occurs between the forward and backward traveling waves. The coupling between them is determined by utilizing the coupled-mode equations:

$$\frac{\partial a}{\partial z} = iK_c \exp(i\Delta\beta z), \tag{2}$$

$$\frac{\partial b}{\partial z} = iK_c \exp(-i\Delta\beta z), \tag{3}$$

where a and b respectively represent the amplitudes of the forward and backward traveling waves, and $\Delta\beta$ is calculated as [14, 15]

$$\Delta\beta = 2\beta - k, \tag{4}$$

where β is the propagation constant of the waveguide, $k=(2\pi)/\lambda$, and K_C is the coupling coefficient, given by

$$K_c = \left(\frac{\pi k_0}{3}\right)\left(\frac{n_2^2-n_1^2}{n_2}\right)\left(\frac{t}{t_g}\right)^3\left[1+\frac{3(\lambda/t)}{2\pi(n_2^2-n_1^2)^{\frac{1}{2}}}+\frac{3(\lambda/t)^2}{4\pi^2(n_2^2-n_1^2)}\right]. \tag{5}$$

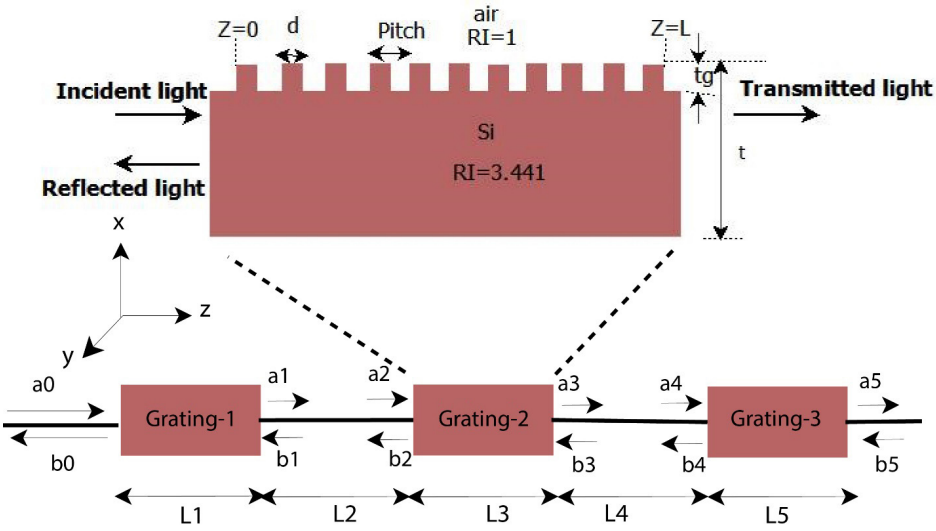

FIG. 2. Superstructure pattern of a surface-relief WBG.

The solution of the coupled-mode equations is given as [14, 15]

$$a(z)=\frac{-\Delta\beta\sinh(\alpha(z-L))+i\alpha\cosh(\alpha(z-L))}{\Delta\beta\sinh(\alpha L)+i\alpha\cosh(\alpha L)}A(0), \tag{6}$$

$$b(z)=\frac{K_c\sinh(\alpha(z-L))}{\Delta\beta\sinh(\alpha L)+i\alpha\cosh(\alpha L)}A(0), \tag{7}$$

where $A(0)$ is the input amplitude and α is given as

$$\alpha=\sqrt{K_c^2-\left(\frac{\Delta\beta}{2}\right)^2}. \tag{8}$$

The transmittance T and reflectance R of the Bragg grating are

$$T=\left|\frac{A(L)}{A(0)}\right|^2, \tag{9}$$

$$R=\left|\frac{B(0)}{A(0)}\right|^2. \tag{10}$$

The superstructure configuration consists of five segments: Grating 1 of length L_1 and Bragg wavelength 1550 nm, Grating 2 of length L_3 and Bragg wavelength 1554 nm, Grating 3 of length L_5 and Bragg wavelength 1557 nm, and two waveguides of length L_2 and L_4 respectively. It is analyzed by the transfer-matrix method for multiple segments [16]:

$$\begin{bmatrix}a(0)\\b(0)\end{bmatrix}=M_1M_2M_3M_4M_5\begin{bmatrix}a(L_5)\\b(L_5)\end{bmatrix}, \tag{11}$$

$$M_i=\begin{bmatrix}\cosh(\alpha_iL_i)+j\frac{\Delta\beta_i}{2\alpha_i}\sinh(\alpha_iL_i) & j\frac{K_{ci}}{\alpha_i}\sinh(\alpha_iL_i)\\ -j\frac{K_{ci}}{\alpha_i}\sinh(\alpha_iL_i) & \cosh(\alpha_iL_i)-j\frac{\Delta\beta_i}{2\alpha_i}\sinh(\alpha_iL_i)\end{bmatrix}, \tag{12}$$

where the index i refers to the i^{th} segment of the superstructure grating. In this case, the second and fourth segments are only a waveguide, so there is no coupling between forward and backward waves; only the forward wave is transmitted. Hence the coefficients M_2 and M_4 are adjusted to replicate a waveguide structure.

3.2. Micromachined Diaphragm

In this section, pressure measurements for two different diaphragm structures, circular and square, are analyzed.

3.2.1. Circular diaphragm

A circular diaphragm with radius f and thickness h is clamped at the edge where $r=f$, as shown in Fig. 3.

The displacement of the diaphragm under pressure p is given by [17]

$$w(r)=\frac{pf^4}{64D}\left(1-\frac{r^2}{f^2}\right)^2. \tag{13}$$

D is the flexural rigidity of the diaphragm, given by

$$D=\frac{Eh^3}{12(1-v^2)}, \tag{14}$$

where E and ν represent the Young's modulus and Poisson's ratio of the diaphragm respectively.

The stresses on the diaphragm are

$$T_r=\frac{3f^2}{8h^2}p\left[(3+v)\frac{r^2}{f^2}-(1+v)\right], \tag{15}$$

$$T_\theta=\frac{3f^2}{8h^2}p\left[(1+3v)\frac{r^2}{f^2}-(1+v)\right], \tag{16}$$

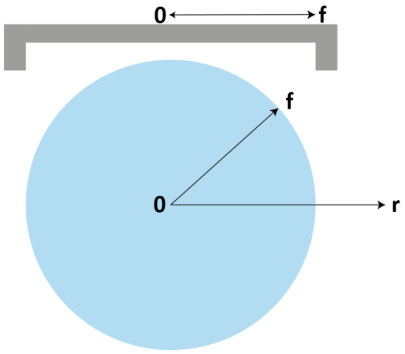

FIG. 3. Schematic diagram of a circular diaphragm.

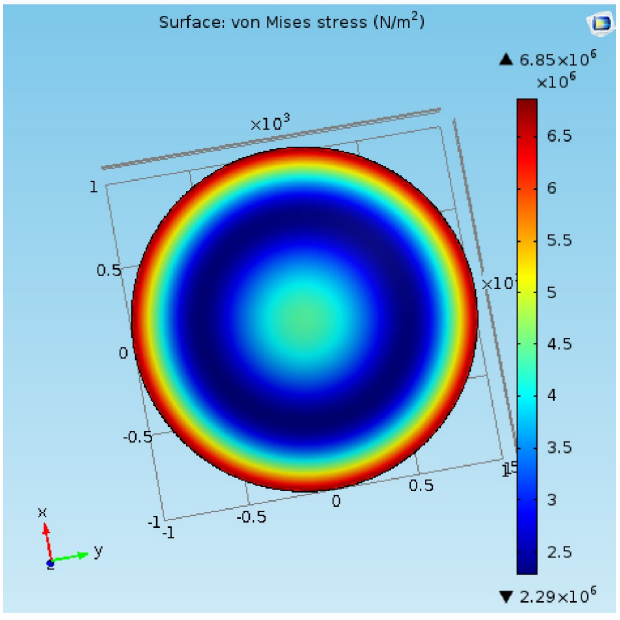

FIG. 4. Stress distribution due to applied pressure on the surface of the circular diaphragm, using COMSOL Multi-physics.

where subscripts r and θ indicate the radial and tangential directions respectively.

The strain components are related to stress as

$$\epsilon_r = \frac{T_r}{E} - v\frac{T_\theta}{E}, \tag{17}$$

$$\epsilon_\theta = \frac{T_\theta}{E} - v\frac{T_r}{E}. \tag{18}$$

Figure 4 shows the stress distribution on the circular diaphragm, when simulated with the COMSOL Multiphysics software package.

The maximum stress of 6.85 MPa is induced the along the perimeter of the circular diaphragm, indicating that this is the ideal location for the grating.

3.2.2. Square diaphragm

A square diaphragm with side length of $2a$ and thickness h under applied pressure is shown in Fig. 5.

The displacement undergone by the diaphragm under pressure p is [17]

$$w(z,y) = 0.0213p\frac{a^4 12(1-v^2)}{Eh^3}\left(1-\frac{z^2}{a^2}\right)^2\left(1-\frac{y^2}{a^2}\right)^2. \tag{19}$$

Displacement of the diaphragm is linearly dependent on the applied pressure, and also varies inversely with the cube of the thickness, so ideally the thickness can be reduced to achieve increased sensitivity (though this also increases the chance of damage to the structure).

The stress distribution across the diaphragm's surface along the z and y axes in Cartesian coordinates zy is

$$T_{zz} = \frac{-0.51pa^2}{h^2}\left[\left(1-\frac{y^2}{a^2}\right)^2\left(1-3\frac{z^2}{a^2}\right)+v\left(1-\frac{z^2}{a^2}\right)^2\left(1-3\frac{y^2}{a^2}\right)\right], \tag{20}$$

$$T_{yy} = \frac{-0.51pa^2}{h^2}\left[\left(1-3\frac{y^2}{a^2}\right)^2\left(1-\frac{z^2}{a^2}\right)+v\left(1-3\frac{z^2}{a^2}\right)^2\left(1-\frac{y^2}{a^2}\right)\right]. \tag{21}$$

The corresponding strain components are

$$\epsilon_{zz} = \frac{T_{zz}}{E} - v\frac{T_{yy}}{E}, \tag{22}$$

$$\epsilon_{yy} = \frac{T_{yy}}{E} - v\frac{T_{zz}}{E}. \tag{23}$$

Stress variation along the length of the square diaphragm is shown in Fig. 6. The maximum stress is found at the edges of the diaphragm.

Figure 7 shows the stress distribution on the square diaphragm, as simulated with COMSOL Multiphysics.

The maximum stress of 22 MPa is induced at the center of each edge of the diaphragm, as seen in Fig. 7. The

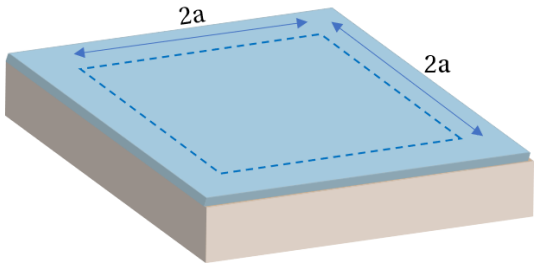

FIG. 5. Schematic representation of a square diaphragm.

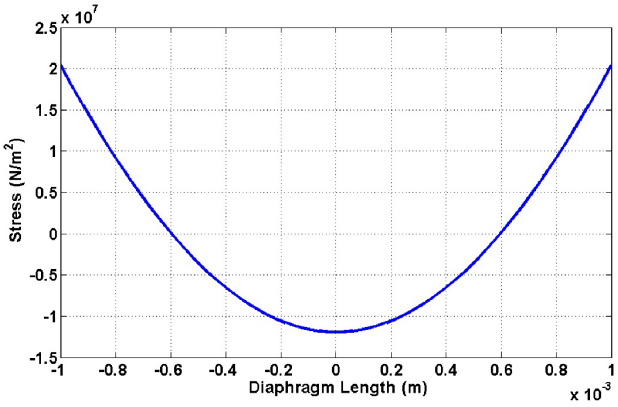

FIG. 6. Stress distribution along the length of the square diaphragm.

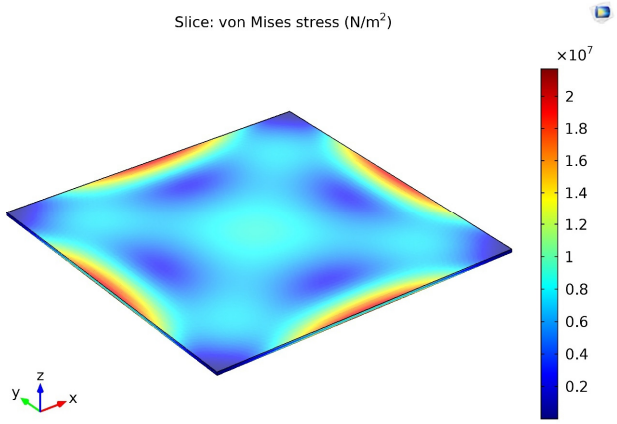

FIG. 7. Stress distribution due to applied pressure on the surface of a diaphragm, using COMSOL Multiphysics.

significantly higher induced stress seen in the square diaphragm makes it a far more effective candidate for pressure sensing than the circular diaphragm, as a higher pressure sensitivity can be obtained. As a consequence, henceforth a square diaphragm is considered for pressure measurement, by placing a grating at the edge of the structure.

With applied stress there is a proportional change in the effective RI and pitch of the grating. Thus Grating 1 in the superstructure shown in Fig. 1 is placed at the edge of

the diaphragm, such that it undergoes a larger change in Bragg wavelength.

3.3. Cantilever Beam

A cantilever beam is shown in Fig. 8, with length, width, and thickness of a_1, b_1, and h_1 respectively. The length, width, and thickness of the proof mass are (a_2-a_1), b_2, and h_2 respectively.

The acceleration is applied in the negative x direction, and the resulting stress is given by [17]

$$T=\frac{6mA(L-z)}{h_1 b_1^2}, \tag{24}$$

where m is the mass of the proof mass, A is the acceleration, and L is $\frac{1}{2}(a_1+a_2)$. The maximum stress occurs at $z=0$, so Grating 2 in the superstructure is placed at this position.

The strain component, which is related to stress, is

$$\epsilon=\frac{T}{E}. \tag{25}$$

The variation in stress along the length of the cantilever beam is plotted in Fig. 9. The maximum stress on the beam is at $z=0$.

Figure 10 shows the stress distribution for the cantilever beam, as simulated using COMSOL Multiphysics.

As seen in Fig. 10, the maximum stress is at the anchor point, so this location is ideal for placement of the grating.

Even though the acceleration is applied along the normal direction (x direction), its effect is also seen in the other directions y and z, and the resulting stresses are shown in Eqs. (26) and (27). This is referred to as cross-axis sensitivity.

$$T_z=\frac{mA}{h_1 b_1}, \tag{26}$$

$$T_y=\frac{6mAL}{h_1 b_1^2}. \tag{27}$$

When comparing the stress in the z direction to the maximum stress in the normal direction, we get $T_z=(h_1/(6L))T$. This gives a very small value of T_z, due to low thickness and large proof mass length, and hence it can be neglected. On the contrary, the stress in the y direction is given by $T_y=(h_1/b_1)T$; this component cannot be neglected, and actually could be considered for some practical applications. This component can be reduced by using a beam of smaller thickness or larger width.

Based on the application, the fundamental frequency of acceleration can be chosen using Eq. (28):

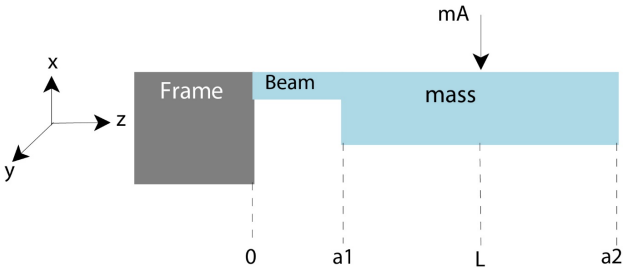

FIG. 8. Schematic diagram of a cantilever beam.

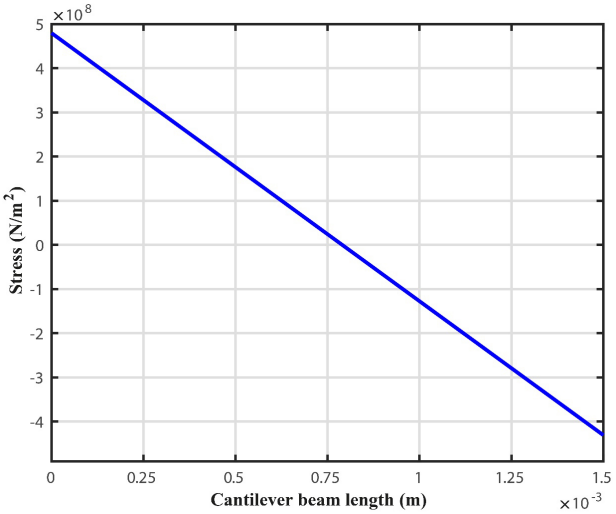

FIG. 9. Stress distribution for the cantilever beam along its length.

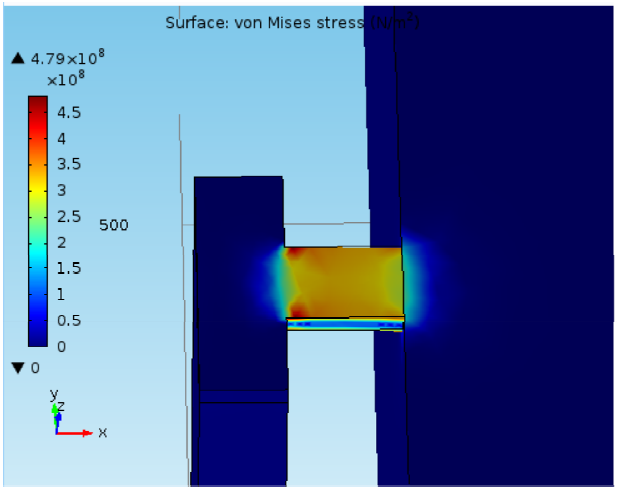

FIG. 10. Stress distribution due to applied acceleration on the surface of the cantilever beam, using COMSOL Multiphysics.

$$f=\frac{1}{8\pi}\sqrt{\frac{Eb_1h_1^3}{mL^2a_1}\left(1+\left(1.25\left(\frac{a_1}{L}\right)+1.08\left(\frac{a_1}{L}\right)^2\right)\right)}. \tag{28}$$

The design parameters used for the structures are outlined in Table 1.

TABLE 1. Design Parameters for the diaphragm and cantilever structures

Design parameter	Value
Waveguide width	460 nm
Waveguide height	220 nm
Waveguide material	Si
Core RI	3.441
Cladding RI	1
Beam height	15 μm
Grating depth	50 nm
Grating pitch	350 nm
Duty cycle	0.5
Grating length	1 mm
Diaphragm length	1 mm
Diaphragm width	1 mm
Diaphragm material	SiO_2
Diaphragm thickness	10 μm
Beam length	80 μm
Beam width	60 μm
Proof mass height	215 μm
Proof mass length	1.5 mm
Proof mass width	1 mm
Cantilever beam material	SiO_2

3.4. Optomechanical Coupling

Under applied pressure and acceleration, stress is induced in both the diaphragm and cantilever beam. This stress causes a change in the effective RI and pitch [18]. Eqs. (29) and (30) respectively quantify these changes in effective RI and pitch for TE-mode (Transverse Electric) analysis of the waveguide on the diaphragm.

$$\Delta n_{eff} = \frac{-n_{eff}^3}{2}(p_{11}\epsilon_{yy} + p_{12}\epsilon_{zz}), \tag{29}$$

$$\Delta\Lambda = \Lambda\epsilon_{yy}, \tag{30}$$

where p_{11} and p_{12} are the stress-optic coefficients. The changes in effective RI and pitch of the grating in the case of the cantilever beam are given by

$$\Delta n_{eff} = \frac{-n_{eff}^3}{2}(p_{11}\epsilon), \tag{31}$$

$$\Delta\Lambda = \Lambda\epsilon. \tag{32}$$

3.5. Temperature Compensation

In a Bragg grating, the wavelength shift depends on both strain and temperature. As a result, it is not possible to measure the pressure or acceleration directly by utilizing a single grating and observing the wavelength shift; it is necessary to compensate for the effect of temperature. In the proposed sensor, we have used another grating on the same waveguide, protected against pressure and acceleration yet at the same temperature as its neighbors. We have designed the superstructure configuration with three surface-relief gratings on the same waveguide and providing reflections at three distinct wavelengths. The wavelength shift in the reflection spectrum in Grating 1 depends on the applied pressure and temperature; similarly, for Grating 2 the shift depends on the acceleration as well as the temperature. On the other hand, the shift for Grating 3 depends on temperature only; as a result, Grating 3 can be used to compensate for the temperature-based shift.

The wavelength shift in the reflection of a grating when it undergoes a change in strain caused by the application of pressure and temperature is given by [19]

$$\Delta\lambda_{B1} = K_p\Delta p + K_T\Delta T, \tag{33}$$

where K_p is the pressure sensitivity coefficient and K_T is the temperature sensitivity coefficient. Δp and ΔT represent the variation in pressure and temperature respectively. Similarly, the wavelength shift of the grating incurred as a result of strain caused by any applied acceleration and temperature is expressed as

$$\Delta\lambda_{B2} = K_{acc}\Delta A + K_T\Delta T, \tag{34}$$

where K_{acc} is the acceleration sensitivity coefficient and ΔA is the change in acceleration.

In our case, we have considered a superstructure of three identical gratings on the same waveguide, but having reflections at three different Bragg wavelengths. The corresponding Bragg-wavelength shifts are given by

$$\Delta\lambda_{B1} = K_{p1}\Delta p + K_{T1}\Delta T, \tag{35}$$

$$\Delta\lambda_{B2} = K_{ac2}\Delta a + K_{T2}\Delta T, \tag{36}$$

$$\Delta\lambda_{B3} = K_{T2}\Delta T. \tag{37}$$

Since the material and the waveguide are common to all the three gratings, we can write

$$K_{T1} = K_{T2} = K_{T3}. \tag{38}$$

The difference between the shifts in wavelength for Grating 1 and Grating 3 cancels out any effect of temperature, and we obtain the shift due to the pressure applied on the diaphragm alone. Similarly, the difference between Grating 2 and Grating 3 wavelength shifts is taken to effectively cancel any temperature effect and capture the acceleration applied to the beam.

IV. RESULTS AND DISCUSSION

Simulations are performed using MATLAB and COMSOL Multiphysics for cases both with and without applied pressure and acceleration. The power-spectral analysis of reflected light for the superstructure WBG sensor without applying any pressure or acceleration is carried out and presented in Fig. 11. Three Bragg-wavelength reflections at 1550 nm, 1553 nm, and 1557 nm were observed, due to the three gratings of different pitch values 348.5 nm, 349.4 nm, and 350 nm respectively.

Figure 12 shows the shifts in the Bragg wavelengths $\Delta\lambda_1$ and $\Delta\lambda_2$ due to simultaneously applied pressure of 7 kPa and acceleration of 2 g on the sensor. Here 1 g equals 9.8 m/s^2. Since there is no variation in temperature, there is no shift in Bragg wavelength of Grating 3; hence overlap of the spectra at its Bragg wavelength is observed.

Figures 13 and 14 show linear variation of Bragg wavelength with pressure and acceleration respectively. Additionally, the pressure sensitivity was obtained as 0.21 pm/Pa, and the sensitivity to acceleration was found to be 6.49 nm/g.

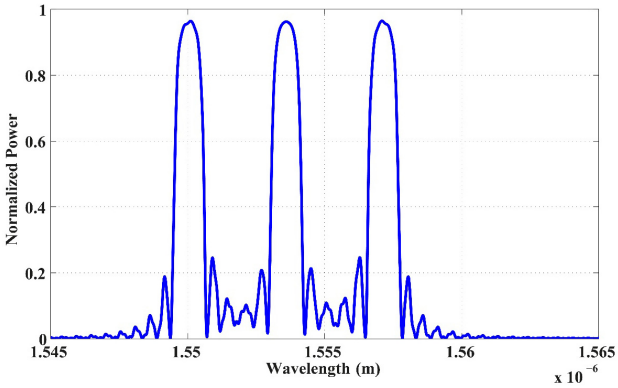

FIG. 11. Reflection spectrum of the superstructure WBG in the steady state.

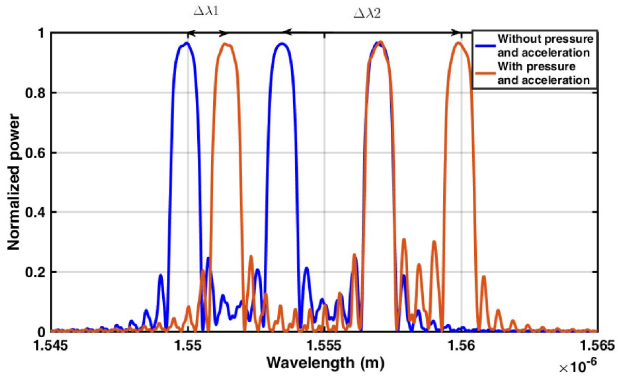

FIG. 12. Reflection spectrum of the superstructure WBG after application of pressure and acceleration.

V. CONCLUSION

We have theoretically analyzed and simulated a temperature-compensated monolithic WBG-based multiparametric sensor for simultaneous measurement of pressure and acceleration, using a unique mathematical model. Three Bragg gratings are used in a superstructure configuration, in which two gratings are used for pressure and acceleration measurement respectively and the remaining one for temperature compensation. A square diaphragm and cantilever beam are designed to obtain high sensitivity. A pressure sensitivity of 0.21 pm/Pa and an acceleration sensitivity of 6.49 nm/g are obtained. Since the fabrication protocols for the proposed superstructured WBG-based sensor fall in line with standard CMOS foundry processes, the device could be integrated at chip scale, with source and detectors on a single chip as a photonic integrated circuit.

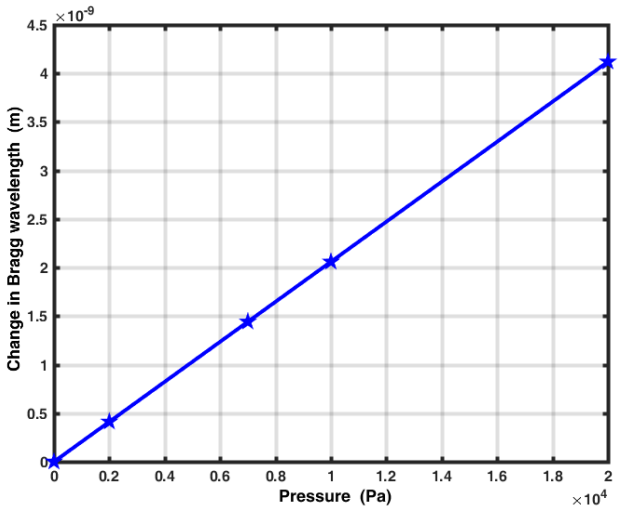

FIG. 13. Change in Bragg wavelength with applied pressure.

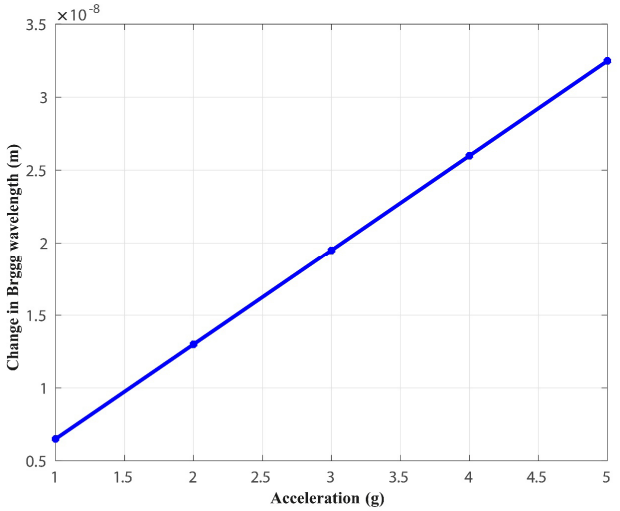

FIG. 14. Change in Bragg wavelength with applied acceleration.

Thus such highly sensitive devices could be an affordable solution for problems where simultaneous measurement of multiple parameters is required.

REFERENCES

1. A. D. Kersey, M. A. Davis, H. J. Patrick, M. LeBlanc, K. P. Koo, C. G. Askins, M. A. Putnam, and E. J. Friebele, "Fiber grating sensors," J. Lightwave Technol. **15**, 1442-1463 (1997).
2. Y. Zhang, D. Feng, Z. Liu, Z. Guo, X. Dong, K. S. Chiang, and B. C. B. Chu, "High-sensitivity pressure sensor using a shielded polymer-coated fiber Bragg grating," IEEE Photonics Technol. Lett. **13**, 618-619 (2001).
3. H. J. Sheng, W. F. Liu, T. C. Chen, S. S. Bor, and M. Y. Fu, "A lateral pressure sensor using a fiber Bragg grating," in *Proc. Pacific Rim Conference on Lasers and Electro-Optics (CLEO)* (Taipei, Taiwan, Dec. 2003), Vol. 2, pp. 674.
4. A. R. Sankar, J. G. Jency, and S. Das, "Design, fabrication and testing of a high-performance silicon piezoresistive Z-axis accelerometer with proof mass-edge-aligned-flexures," Microsyst. Technol. **18**, 9-23 (2012).
5. D. Feng, X. Qiao, H. Yang, Q. Rong, R. Wang, Y. Du, M. Hu, and Z. Feng, "A fiber Bragg grating accelerometer based on a hybridization of cantilever beam," IEEE Sens. J. **15**, 1532-1537 (2015).
6. J. Dong, Z. J. Long, H. Jiang, and L. Sun, "Monolithic-integrated piezoresistive MEMS accelerometer pressure sensor with glass-silicon-glass sandwich structure," Microsyst. Technol. **23**, 1563-1574 (2017).
7. J. Xu, Y. Zhao, Z. Jiang, and J. Sun, "A monolithic silicon multi-sensor for measuring three-axis acceleration, pressure and temperature," J. Mech. Sci. Technol. **22**, 731-739 (2008).
8. P. K. Pattnaik, B. Vijayaaditya, T. Srinivas, and A. Selvarajan, "Optical MEMS pressure and vibration sensors using integrated optical ring resonators," in *Proc. SENSORS* (Irvine, CA, USA, Nov. 2005), pp. 636-639.
9. G. N. D. Brabander, J. T. Boyd, and G. Beheim, "Integrated optical ring resonator with micromechanical diaphragm for pressure sensing," IEEE Photonics Technol. Lett. **6**, 671-673 (1994).
10. C. Thondagere, A. Kaushalram, T. Srinivas, and G. Hegde, "Mathematical modeling of optical MEMS differential pressure sensor using waveguide Bragg gratings embedded in Mach Zehnder interferometer," J. Opt. **20**, 085802 (2018).
11. É. Pinet, "Pressure measurement with fiber-optic sensors: commercial technologies and applications," Proc. SPIE **7753**, 775304 (2011).
12. S. Kim, J. Kwon, S. Kim, and B. Lee, "Temperature-independent strain sensor using a chirped grating partially embedded in a glass tube," IEEE Photonics Technol. Lett. **12**, 678-680 (2000).
13. V. Neeharika and P. K. Pattnaik, "Optical MEMS pressure sensors incorporating dual waveguide Bragg gratings on diaphragms," IEEE Sens. J. **16**, 681-687 (2016).
14. C. R. Pollock and M. Lipson, "Coupled mode theory," in *Integrated Photonics* (Springer US, 2003), pp. 241-269.
15. A. Yariv, "Coupled-mode theory for guided-wave optics," IEEE J. Quantum Electron. **9**, 919-933 (1973).
16. A. Yariv and P. Yeh, "Wave propagation in periodic media," in *Photonics: Optical Electronics in Modern Communications (Oxford Series in Electrical and Computer Engineering)*, A. S. Sedra, ed., 6th ed. (Oxford University Press, NY, USA, 2007), pp. 539-601.
17. M. H. Bao, "Basic mechanics of beam and diaphragm structures," in *Micro Mechanical Transducers: Pressure Sensors, Accelerometers and Gyroscopes (Handbook of Sensors and Actuators Series)*, S. Middelhoek, ed. (Elsevier, The Netherlands, 2000), Vol. 8, pp. 23-88.
18. C. Holmes, "Direct UV written planar devices for sensing and telecommunication applications," Ph. D. Dissertation, University of Southampton, Southampton (2009).
19. M. M. Werneck, R. C. S. B. Allil, B. A. Ribeiro, F. V. B. D. Nazare, "A guide to fiber Bragg grating sensors," in *Current Trends in Short-and Long-period Fiber Gratings*, C. C. Laborde, ed. (InTech, Rijeka, Croatia, 2013), pp. 2-24.